Chapter 6

Using the Light Scattering Component of Optical Intrinsic Signals to Visualize In Vivo Functional Structures of Neural Tissues

Uma Maheswari Rajagopalan, Kazushige Tsunoda, and Manabu Tanifuji

Abstract

Visualization of changes in reflected light from *in vivo* brain tissues reveals spatial patterns of neural activity. An important factor which influences the degree of light reflected includes the change in light scattering elicited by neural activation. Microstructures of neural tissues generally cause light scattering, and neural activities are associated with some changes in the microstructures. Here, we show that the optical properties unique to light scattering enable us to visualize spatial patterns of retinal activity non-invasively (FRG: functional retinography), and resolve functional structures in depth (fOCT: functional optical coherence tomography).

Key words: Intrinisic signal imaging, OCT, optical coherence tomography, light scattering.

1. Introduction

In 1986, Blasdel and Salame visualized orientation columns in monkey visual cortex *in vivo* by staining the brain surface with a voltage-sensitive dye and observed spatial patterns of absorption changes elicited during visual stimuli *(1)*. After this initial finding, it has been shown that functional structures can also be visualized intrinsically, by measuring changes in light reflection without the need for dyes *(2)*. This technique, the measurement of intrinsic reflection changes elicited by neural activation, is called optical intrinsic signal imaging (OISI), and is widely used to map cortical functional structures in neural tissues of living animals *(3–9)*. Because the intrinsic signals were originally found as byproduct

Fahmeed Hyder (ed.), *Dynamic Brain Imaging: Multi-Modal Methods and In Vivo Applications, vol. 489*

DOI 10.1007/978-1-59745-543-5_6 Springerprotocols.com

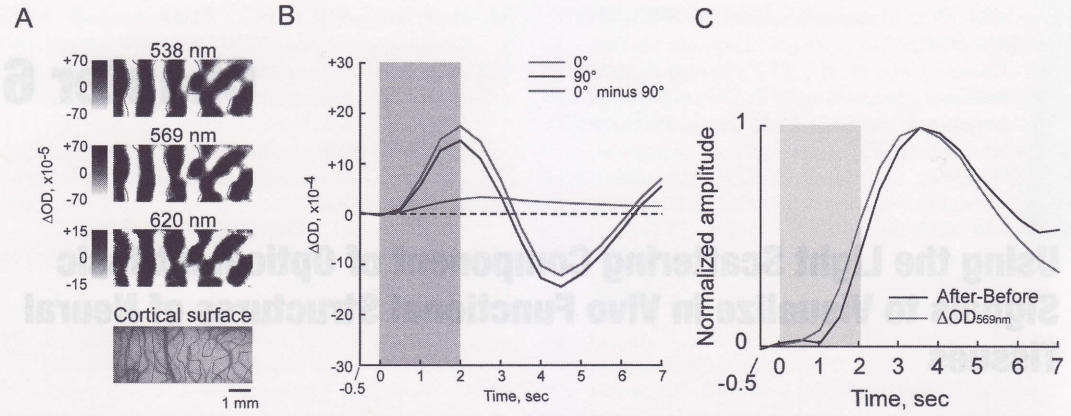

Fig. 6.1. Orientation columns visualized by OISI at different wavelengths. Typically in visual cortex, intrinsic signals consist of stimulus-specific and -nonspecific components. Orientation columns are reflected in the stimulus-specific component that is a local modulation of a stimulus-nonspecific component. In (A), we subtracted activation patterns obtained by one stimulus (90 deg. orientation) from the other (0 deg. orientation) to remove stimulus-nonspecific components. Please note that, depending on the size of the functional structures of interest, stimulus specificity of synaptic inputs, and spread of intrinsic signals, distinction between stimulus-specific and nonspecific components may not be required (for example, see **Figs. 6.3 and 6.4**). Columnar patterns obtained at different wavelengths are nearly the same as indicated by contours in red drawn for columnar patterns obtained at 620 nm. Although it is not shown here, similar patterns of functional structures were also observed using infrared light. Bottom image shows vessel patterns of the exposed cortical surface where the above recordings were made. (B) Time courses of stimulus-nonspecific (red and blue lines) and stimulus-specific (green line) components obtained at 620 nm. Increase of ΔOD corresponds to increase of deoxyhemoglobin. The visual stimulus was given from 0 to 2 s. (C) Time course of stimulus-nonspecific components obtained at 570 nm (Green line). The black line indicates time course of blood volume changes estimated by subtraction between time courses obtained before and after the extrinsic absorption dye infusion into the blood stream (see Fukuda et al., 2005 for details). The visual stimulus was given from 0 to 2 s. (*See* Color Plate)

of dye-sensitive absorption changes, the sources of these signals have since been debated.

One unique feature of OISI is that functional structures produce nearly identical spatial activation patterns at a wide range of imaging wavelengths (**Fig. 6.1A**). The dominant sources of intrinsic signals, however, differ from wavelength to wavelength. At least three components are involved in intrinsic signals, and all of them are secondarily elicited by neural activations. These components are changes in the oxygenation levels of hemoglobin, changes in blood volume within neural tissues, and changes in microstructures of neural tissues.

Oxy- and deoxygenated hemoglobin in blood vessels are the major light absorbing molecules in neural tissues at around 500–650 nm. Particularly, changes in the oxygenation level of hemoglobin are considered the major source of intrinsic signals around 610 nm because light absorption is dominated by deoxyhemoglobin at this wavelength. Vanzetta and Grinvald recorded changes in tissue oxygen tension by measuring changes in phosphorescence of an oxygen-sensitive dye *(10)*. They found that oxygen tension initially decreases within 2 s after stimulus onset, and then increases beyond the baseline oxygen tension during

persistent stimulation. This time course of changes in oxygen tension was quite consistent with the time course of intrinsic signals (stimulus-nonspecific component) observed at 620 nm (**Fig. 6.1B**). This result provides good evidence that the deoxygenation level of hemoglobin is one of the sources of intrinsic signals.

A second source of intrinsic optical signals stems from changes in blood volume within neural tissues. One of the isosbestic points of oxy- and deoxy-hemoglobin absorption is located at 570 nm within the major absorption spectrum band. Thus, the intrinsic signals at this wavelength should be dominated by changes in blood volume in tissue blood vessels. Several studies provide supporting evidence for the involvement of blood volume changes in intrinsic signals *(11, 12)*. For example, infusion of extrinsic absorption dye into the blood stream increases absorption changes elicited by neural activation at the wavelength specific for that dye, and the time course of the signal was nearly identical to the time course of intrinsic signals recorded at 570 nm, where blood volume changes seem to dominate (**Fig. 6.1C**) *(12)*.

Microstructures of neural tissue, such as intricate subcomponents of neurons, multiple types of glial cells, and collection of blood vessels of various sizes generally cause scattering of light that penetrates the neural tissues. If neural activities are associated with changes in these microstructures, then light scattering changes from intrinsic signals could be a component for neuroimaging.

Changes in tissue light scattering is indeed considered a source of intrinsic signals since intrinsic signals are also observed at the wavelengths outside of the major band of the hemoglobin absorption spectrum. The light scattering component of the intrinsic signal has unique properties that do not exist in the absorption of oxy- and deoxy-hemoglobin. First, we can detect light scattering changes at a wide range of wavelengths, including infrared light, where hemoglobin absorption is minimal. Using light scattering in the infrared offers several advantages. Infrared light permits visualization of functional signals from tissues sensitive to visible light, such as the retina, as well as detection of signals from deeper structures because of the increased light penetration in the infrared light range compared to the visible range. Second, we can detect light scattering changes not only through changes in light reflection but also through phase-sensitive detection such as optical coherence tomography (OCT), which enables us to resolve functional structures in greater depth. Finally, light scattering changes may have faster time courses than the other intrinsic signals, allowing us to resolve neural events with higher temporal resolution than signals originating from hemodynamics. Nevertheless, firm evidence

for the contribution of the light scattering changes has not been demonstrated until recently. Here, we will focus on the light scattering component of intrinsic signals. In particular, we will show evidence for the involvement of light scattering changes in intrinsic signals, applications of OISI to functional imaging of the retina using the light scattering component, and depth-resolved functional imaging with OCT.

2. OISI for Functional Imaging from Retina (Functional Retinography)

With the increasing number of people suffering from vision-threatening retinal diseases, such as age-related macular degeneration, there is an urgent need for the development of objective methods to measure retinal function, by which functional disorder can be detected before symptomatic or structural changes occur. The distribution of retinal responsiveness could not be adequately mapped by conventional techniques, such as electroretinogram (ERG). Therefore, we have developed a recording system for measuring flash-evoked intrinsic signals from the macaque retina *(13, 14)*.

We have applied OISI to macaque retina, and successfully demonstrated the topography of cone- and rod-induced neural function by measuring the light reflectance changes following flash stimulus. Because of the differences in anatomical structures, the properties of intrinsic signals in retina are quite different from those in the cerebral cortex. Here, we will focus on the light reflectance changes in two discrete regions in the posterior retina: fovea and posterior retina apart from the fovea (perifoveal regions).

The ocular fundus of Rhesus monkey under anesthesia was monitored via a modified fundus camera equipped with a CCD camera (**Fig. 6.2**). The intrinsic signals evoked by white diffuse flash stimuli were calculated by dividing the averaged images obtained after the flash by those obtained before the flash *(13, 14)* (see details in Appendix 1). With an observation light wavelength of 630 nm, the light reflectance from the fovea increased (retinal image became brighter), whereas, the light reflectance from the perifoveal regions decreased (retinal image became darker) following a flash stimulus (**Fig. 6.3A**). The increase in light reflectance following a flash in the foveal region was attributed to the bleaching of photopigments by visible light *(15–18)*. On the other hand, the decrease in light reflectance in the perifoveal region was attributed to the hemoglobin-related reflectance changes or tissue light scattering changes, which can be observed in the cerebral cortex *(13)*. The pseudocolor map (**Fig. 6.3A**) shows that the signals in the foveal and perifoveal

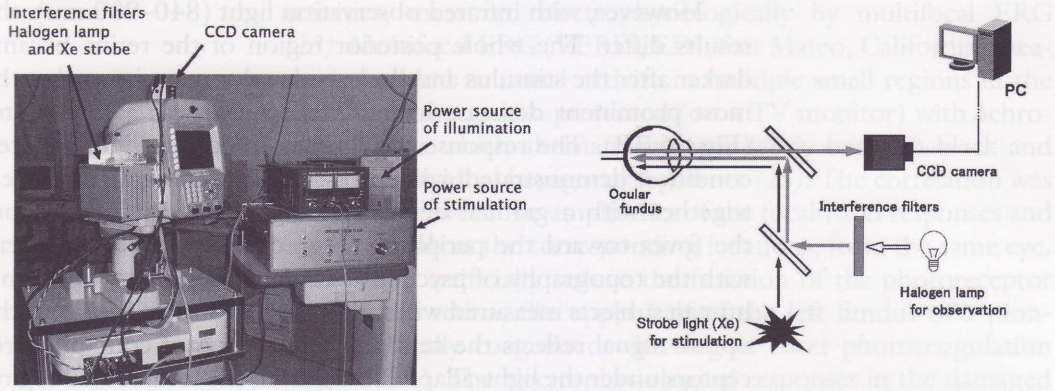

Fig. 6.2. Overall view of the intrinsic signals imaging system for retina (left) and schematic drawing of the experimental setup (right). Throughout the recording trial, the fundus was continuously illuminated with observation light through one of the bandpass filters. (*See* Color Plate)

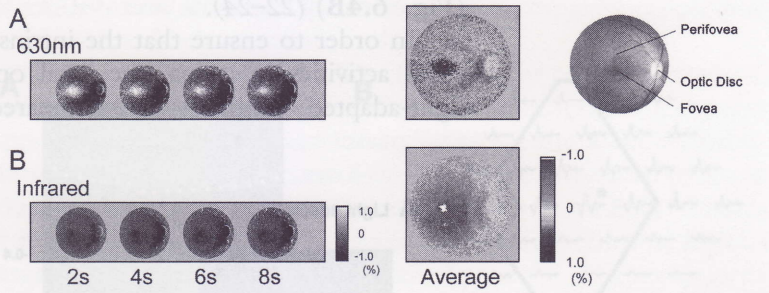

Fig. 6.3. Time courses of two-dimensional images of retina showing light reflectance changes following a flash stimulus observed with 630 nm (**A**) and infrared (**B**) light, measured in the posterior pole region of normal retina. The averaged reflectance changes during the first second after the flash are shown in pseudocolor maps on the right. Color indicates relative light reflectance changes from pre-stimulus level. Fundus photograph of a normal macaque retina is shown in the right. (*See* Color Plate)

regions have different polarities. In the foveal region, the contribution of brightening by photopigment bleaching is greater than that of darkening by light scattering changes.

In retinal optical imaging, we need to take into account two points when visible light is used for OISI: (1) Visible light for observation evokes neural activity and the reflectance can be changed without giving flash stimuli. The baseline retinal reflectance is thus unstable during recording.(2) Following bleaching of photopigments under visible light, the foveal reflectance is dramatically increased (retinal image becomes brighter) and this bleaching-related reflectance change has an opposite polarity to conventional intrinsic signals, which are commonly observed as decreases in light reflectance (retinal image becomes darker).

However, with infrared observation light (840–900 nm), the results differ. The whole posterior region of the retina became darker after the stimulus and the pseudocolor map shows that the most prominent decrease in light reflectance was at the center (**Fig. 6.3B**). The response topography under the light-adapted condition demonstrated a steep peak of darkening at the fovea, together with a gradual decrease of signal intensity away from the fovea toward the periphery (**Fig. 6.4A**). This is consistent with the topography of psychophysical cone sensitivity in normal human subjects measured with bright background *(19–21)*. If the optical signal reflects the central accumulation of cone photoreceptors under the light-adapted condition, the local retinal region with high rod density, called the 'rod ring', should also be activated under the dark-adapted condition. Following forty minutes of dark adaptation, the intrinsic signal showed additional peaks along the circular region surrounding the macula at the eccentricity of the optic disk, together with the central peak at the fovea (**Fig. 6.4B**) *(22–24)*.

In order to ensure that the intrinsic signals reflect the neuronal activities in retina, the local optical signal values under light-adapted condition were compared with the local neuronal

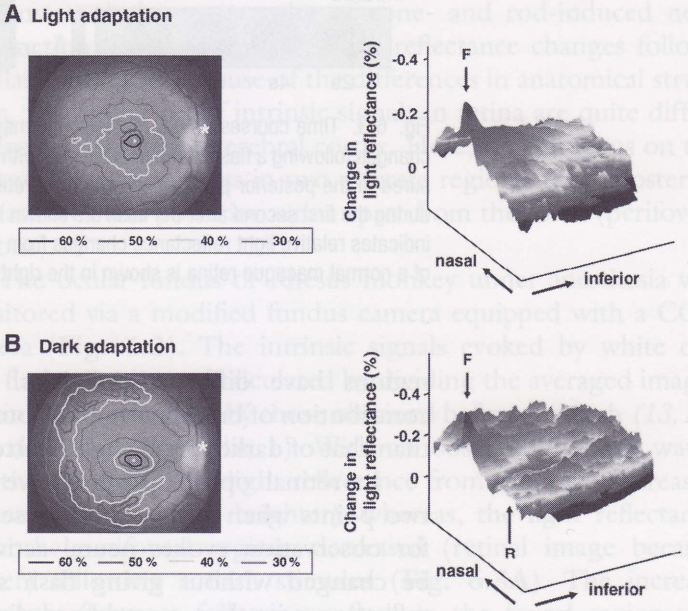

Fig. 6.4. Response topography of normal retina under light-adapted (**A**) and dark-adapted (**B**) conditions. The foveal center is indicated by a white dot and the optic disk is indicated by an asterisk. Regions with 60%, 50%, 40% and 30% of the peak signal intensity value at the fovea were outlined by different colors. Pseudocolor topographic maps of light reflectance changes in the inferior retina, profiled along the horizontal meridian, are shown on the right. The location of the fovea is indicated by F, and the crest of 'rod ring' is indicated by R. (*See* Color Plate)

activities, measured electrophysiologically by multifocal ERG *(13)*. Multifocal ERG (VERIS, EDI, San Mateo, California) measures the local neuronal activity in multiple small regions in the posterior retina, when presented (on a TV monitor) with achromatic flicker which alternates independently between black and white in individual hexagonal segments *(25)*. The correlation was evaluated between the amplitudes of the focal ERG responses and optical signals at the corresponding locations, from the same eye. In order to artificially reduce the function of the photoreceptor layer of the retina, the upper half of the left fundus of a monkey was locally coagulated with Argon Laser photocoagulation (**Fig. 6.5A**). The electrophysiological responses in the damaged region were reduced accordingly (**Fig. 6.5B**). In intrinsic signal imaging, the damaged region also showed smaller amount of light reflectance decrease (**Fig. 6.5C**). The light reflectance decrease and the multifocal ERG signal showed statistically significant positive correlation ($r^2 = 0.79$, $p < 0.001$, $n = 45$) (**Fig. 6.5D**). The

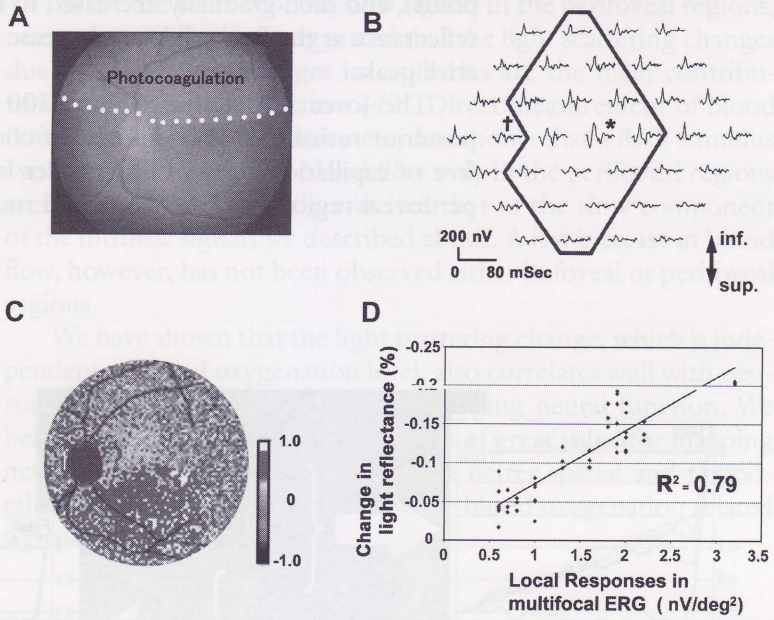

Fig. 6.5. (**A**) Photograph of the monkey's retina artificially damaged by Argon Laser Photocoagulation. The upper half of posterior retina was densely coagulated, sparing the macular area. (**B**) Array of 37 local responses of multifocal ERG, taken from the fundus in (**A**). ERGs with ∗ and † indicate the location of macula and optic disk, respectively. Note that the responses of the intact retina in the lower half region are inversely shown in the upper half of the arrays. (**C**) pseudocolor map of flash-evoked intrinsic signals measured with infrared light. Red color indicates light reflectance decrease (*darkening*) from pre-stimulus level. Flash-evoked darkening could not be observed in the damaged region (*upper half*). (**D**) Correlation between the change in light reflectance decrease and the focal responses in ERG at the corresponding retinal location under infrared light. Correlation coefficient: $r^2 = 0.79$ ($p < 0.001$, $n=45$). (*See* Color Plate)

results of optical imaging and electrophysiological measurement were well correlated not only in their response amplitudes but also in the spatial location of reduced responses: the border between normal and reduced response regions in both measurements corresponded to the border between normal site and photocoagulation site.

Interestingly, with infrared observation, the time course of the intrinsic signals evoked by a brief flash stimulus was different for different regions of the ocular fundus. Representative time courses of flash-evoked response at the foveal and perifoveal regions under the dark-adapted condition are shown in **Fig. 6.6**. The reflectance changes at the fovea were rapid and reached a negative peak (darkening) within 100 to 200 ms following the flash. The darkening then gradually returned toward the pre-stimulus baseline. The signals in the perifoveal regions (3°–12°) were composed of both fast and slow components. The time courses of the intrinsic signals of the perifoveal regions were approximately the same and distinct from the foveal response: the light reflectance decreased rapidly within 100 ms (flexural point), and then gradually decreased to reach a trough. The light reflectance at the fovea did not decrease following the initial negative peak.

The fovea is a central region (300 μm in diameter) in the posterior retina that is composed of cone photoreceptors and is free of capillaries and middle or inner layer structures *(26)*. The perifoveal region has both cone and rod photoreceptors, and its

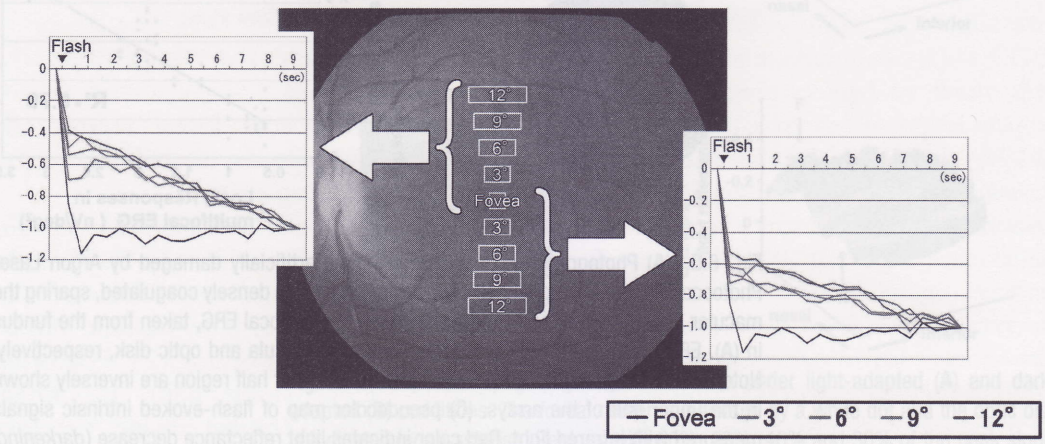

Fig. 6.6. Time courses of light reflectance changes in a single trial following a diffuse flash, measured at the fovea and different regions within twelve degrees superior or inferior to the fovea. Amplitudes are indicated as values relative to the light reflectance changes at the end of each trial (1.0). The four regions tested in each quadrant are indicated as distances from the fovea (3,6,9 and 12°). (*See* Color Plate)

inner and middle layers are nourished by retinal vessels and capillaries. We believe that the light scattering changes following activation of the cone photoreceptors are probably the source of the fast intrinsic signals observed at the fovea because the foveal avascular region is not subject to changes in hemoglobin concentration or blood volume following neural activation *(14)*. The rapid darkening observed at the perifoveal regions may also be derived from light scattering changes because, under infrared light, the change in the optical signal due to deoxygenated hemoglobin concentration is thought to be much smaller than that from tissue light scattering *(27)*. The light scattering changes following a flash are thought to be derived from microstructural changes in the outer segment disks, membrane hyperpolarization, cell swelling, and changes in the composition of the inter-photoreceptor matrix. Recent functional OCT studies using blood-free slice preparations *(28,29)* or in vivo retina *(30)* showed that the reflectance in the photoreceptor layer is strongly modulated by neural activation followed by microscopic morphological changes.

As for the sources of the slow signals in the perifoveal regions, our recent studies have suggested that the light scattering changes due to blood flow changes in capillaries are the main contributors to changes in reflectance *(42)*. Direct measurement of blood flow with laser Doppler flowmetry has shown that a flash stimulus evokes a slow increase in blood flow only in the perifoveal regions and its time course exactly matched that of the slow component of the intrinsic signals we described above. A fast increase in blood flow, however, has not been observed either in foveal or perifoveal regions.

We have shown that the light scattering change, which is independent of blood oxygenation level, also correlates well with neuronal activity and can be used for mapping neural function. We believe that this fast scattering signal is of great value for mapping neuronal activity because it may have better spatial and temporal resolutions than the blood-flow- or blood oxygenation related signals.

3. Optical Coherence Tomography (OCT) for Functional Imaging Resolved in Depth (Functional OCT)

In conventional OISI with CCD cameras, the measured reflected light is actually the integrated signals over depths determined by the collection optics. Hence potential variations in functional organization across depth may go undetected. Optical coherence tomography (OCT) is an optical imaging technique that has the potential to show reflectivity at specific depths because the method is a sensitive measure of refractive index variations across

depth *(31,32)*. In this technique, light from a low-coherence light source is focused onto the tissue and reflectivity of the internal microstructures at different depths is measured by an interferometer, thus providing a map of the structural profile of the tissue. As described in the previous section on conventional OISI, in addition to the oxy- and deoxy-hemoglobin related absorption changes, scattering changes also contribute to the intrinsic signal measured with OCT. Scattering changes could result from changes in the size of the scatterer or the density of the scatterer, or both. During neural activation, secondary physiological structural changes such as those in photoreceptors described above *(13)*, capillary dilation *(12,33)*, change in the density of red blood cells *(34)* and swelling of glial cells *(35)* can occur *(36)*. We expect that the changes in scattering characteristics would result in an activity-dependent reflectivity change, and that the sensitivity of OCT to refractive index changes would make it theoretically sensitive to the scattering changes such as those happening during neural activation. We refer to this technique as functional OCT (fOCT) and its signal as fOCT signal.

To demonstrate the potential of OCT in functional studies, we used primary visual cortex (V1) of cats to confirm that detection of a stimulus-specific reflectivity change is feasible *(36, 37)*. The reliability of the technique was demonstrated by comparison with results of conventional OSIS and multi-unit activity recorded electrophysiologically. Recently, supporting evidence for the potential of OCT in functional studies has been reported in squid *(38)* and in retina *(28–30)*.

4. Brief Introduction for Optical Coherence Tomography (OCT)

Figure 6.7A shows a simple schematic of the principles of an interferometer: a broad-spectrum light source is divided by a half mirror into two beams, one illuminating the reference mirror and the other illuminating a turbid medium such as the cortex. The light reflected back from the reference mirror and the cortex are recombined at the half mirror to reach the detector. The reflected light beams would interfere only if their total light path length difference (Lr-Ls) is within the coherence length of the source, or, in other words, if the light reaching the detector has temporal correlation. The extent of temporal correlation is determined by autocorrelation of the source, and can be described in terms of the spectral width (Proportional to $\lambda_0^2/\Delta\lambda$) of the source, where λ_0 is the central mean wavelength and $\Delta\lambda$ the spectral width. For the case of the light source used in OCT, the coherence length is on the order of a few μm to a few tens of μm. So, by having a mechanism to move the reference mirror, it is possible to dissect

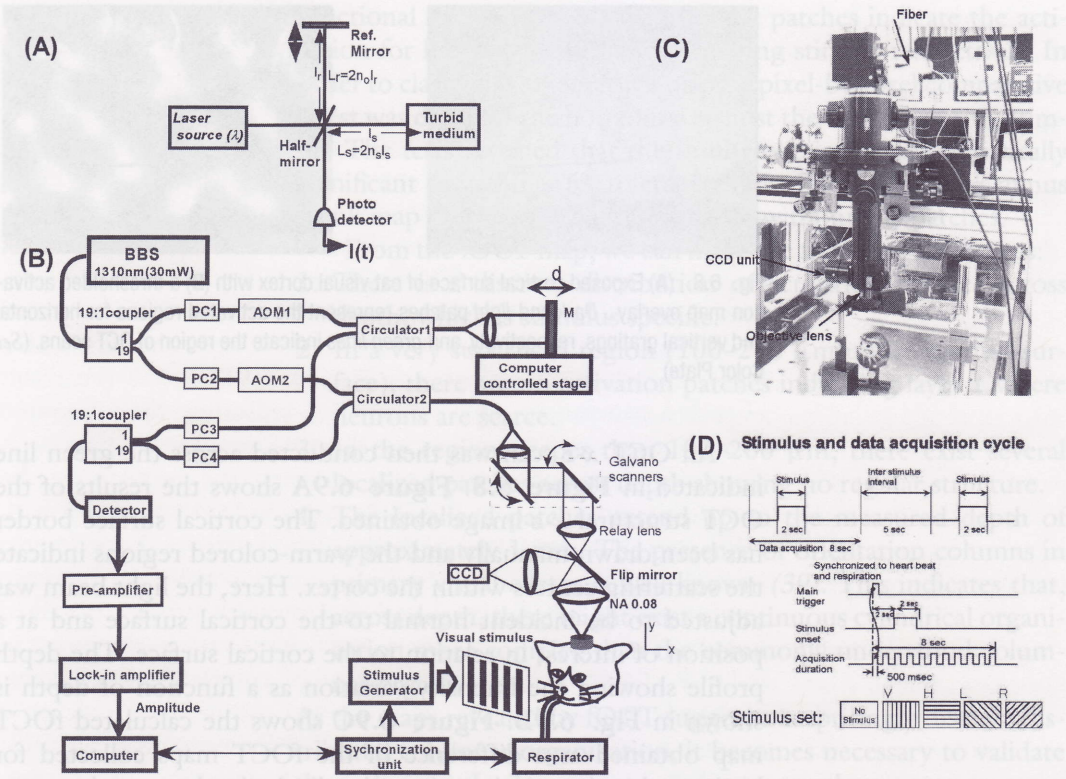

Fig. 6.7. A schematic of the basic principle of OCT (**A**) and the experimental system used (**B**) along with a picture of the probe unit (**C**) and a schematic of the scanning paradigm (**D**). In the figure (**B**), the abbreviations denote: BBS - Broad Band Source, AOM- Acousto-Optic Modulator, PC - Polarization Controller, M – Mirror and O – Objective lens. (*See* Color Plate)

the cortex optically and obtain depth-resolved reflectivity maps. The experimental system used in our studies and other details are described in Appendix 2.

5. Functional Imaging with OCT (fOCT)

Prior to doing functional imaging with OCT, we performed in vivo optical intrinsic signal imaging with the exposed cortical surface of cat visual cortex (**Fig. 6.8A**) at a wavelength of 607 nm. The stimulus set was identical to the one used in fOCT. It consisted of four differently oriented gratings and a blank screen used as a control (see detailed protocol in Appendix 2). **Figure 6.8B** shows the thresholded difference maps obtained when horizontal and vertical grating visual stimuli were presented to the cat. Dark and bright regions indicate the activated regions for horizontal and vertical gratings, respectively.

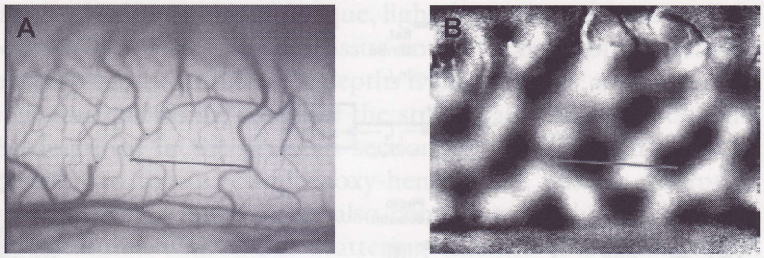

Fig. 6.8. (**A**) Exposed cortical surface of cat visual cortex with (**B**) a thresholded activation map overlay . *Dark* and *light* patches represent the activated regions for horizontal and vertical gratings, respectively, and *green lines* indicate the region of OCT scans. (*See* Color Plate)

An OCT *x*-*z* scan was then conducted across the green line indicated in **Figure 6.8**. **Figure 6.9A** shows the results of the OCT structural *x*-*z* image obtained. The cortical surface border has been drawn manually and the warm-colored regions indicate the scattering centers within the cortex. Here, the light beam was adjusted to be incident normal to the cortical surface and at a position of interest in relation to the cortical surface. The depth profile showing the intensity variation as a function of depth is shown in **Fig. 6.9B**. **Figure 6.9C** shows the calculated fOCT map obtained as a difference of the fOCT maps collected for horizontal and vertical grating stimuli obtained across the green line of **Fig. 6.8** (see Appendix 2 for calculation used to extract

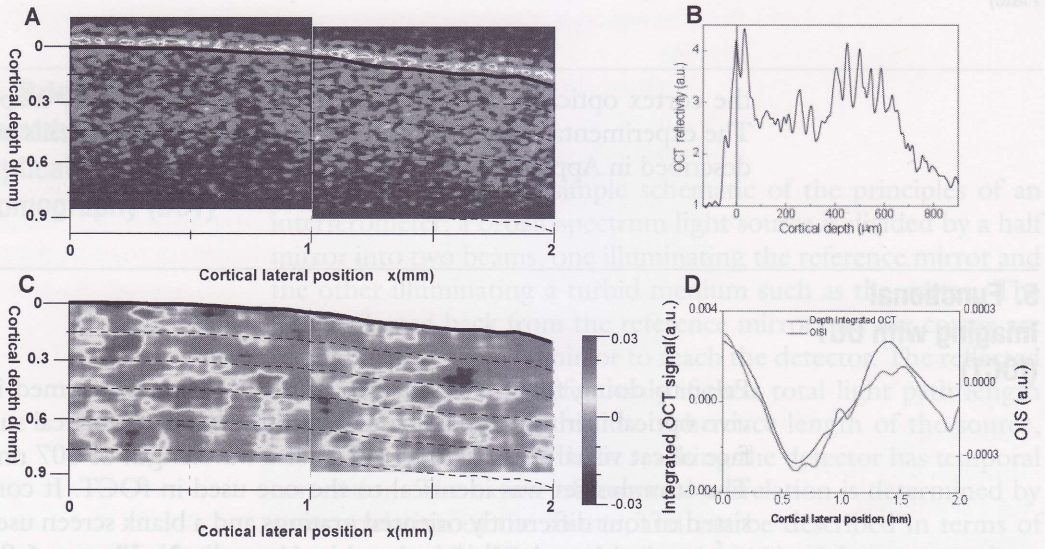

Fig. 6.9. (**A**) OCT scan obtained across the line indicated in Fig. 6.8 with (**B**) a typical depth reflectivity profile from (**A**) and the corresponding (**C**) Functional OCT map and (**D**) Consistency of OISI result with the integrated result of fOCT. In (**C**), *red* and *blue* patches represent the activated regions for horizontal and vertical gratings, respectively. In (**D**) green line indicates the variation of OISI across the line indicated in Fig. 6.8B. while the *red line* obtained by calculating the functional signal from integrating the OCT scans across the full scanned depth range of Fig. 6.9A. (*see* Color Plate)

functional signals). Here, red and blue patches indicate the activation for horizontal and vertical grating stimuli, respectively. In order to clarify the reliability of maps, a pixel-by-pixel comparative t-test was done for the horizontal against the vertical grating stimuli. The tests revealed that the results obtained were statistically significant to within a 5% tolerance limit. Further, a blank minus blank map did reveal a flat distribution without any patches.

From the fOCT map, we can make the following inferences:

1. There is a discrete distribution of activation patches across depth, which is stimulus specific.
2. In a very superficial region (100–200 μm under cortical surface), there are no activation patches indicating layer 1 where neurons are scarce.
3. In the region deeper than 100–200 μm, there exist several localized patches across depth showing no regular structure.
4. The localized patches extend up to the measured depth of approximately 1 mm. The presence of orientation columns in primary visual cortex is well known *(39)*. This indicates that, across depth, there might exist a continuous cylindrical organization more complex than the commonly understood columnar organization.

As the maps revealed by fOCT suggest a surprisingly discrete distributed columnar organization, it becomes necessary to validate the technique. In the present measurements, there are two potential issues that need to be considered:

1. Although we could observe a functional signal that arises as a result of scattering change due to neural activation, it is still not possible to specify the origin regarding the exact nature of the scattering changes such as glial swelling or capillary dilation. One way to resolve this issue may be to increase the spatial resolution of the technique, a possibility that is technically feasible. But even with increased resolution, allowing us to visualize the details of the structural organization, it is still not clear whether the reflectivity changes could provide enough contrast to resolve finer details such as neuronal cells, glial cells and blood vessels etc. To resolve such structural differences, one way is by specifically attaching contrast agents such as gold particles to specific structures such as neurons. We previously proposed a method of increasing the reflectivity in OCT *(40)* by introducing properly sized gold particles. With such specific labeling, we may be able to increase the reflectivity from specific structures, which would, in turn, enable us to specify the origin of scattering change.
2. Another issue is that the site of localized scattering change may not correspond to the site of neural activity. To address this problem, we conducted electrophysiology recordings to measure the neuronal activity at the sites revealed by fOCT discussed in the following section.

6. Reliability of the Signal as a Measure of Localization of Neural Activity

As the correlation of OISI maps with neural activity is already well established *(3, 4, 41)*, a comparison of fOCT with OISI is a reasonable validation approach. We compared the intensity variation of an OISI map across the scanned line (**Fig. 6.8**) with the integrated profile of fOCT. In order to calculate the integrated profile, all the pixels across the z-direction were summed to obtain a profile that varies only across x; then the differential OCT at each x was calculated. **Figure 6.9D** shows the result of such a comparison with the red line indicating the integrated result and green line indicating the OIS intensity variation. A clear and remarkable agreement between the profiles can be seen. This indicates that fOCT signal is indeed correlated with OISI and thus correlated with the neural activity. Experiments were done in 5 cats and showed a good correlation between the integrated fOCT signal and the intensity profiles obtained from intrinsic maps. Correlation coefficients vary in the range of 0.3–0.9. **Table 6.1** gives the results of correlation coefficients obtained from a cat from different scan positions. However, a general caveat is that there are many differences between OISI and fOCT, including illumination and detection geometries, wavelengths used and the origin of the signals. In fOCT, as near-infrared wavelength is used, oxy- and deoxy-hemoglobin have almost the same absorption coefficients and hence the absorption changes are minimal. The main source of the signal is thought to be scattering changes. Nevertheless, the OISI results corresponded very well with the integrated profiles of fOCT.

Table 6.1
The correlation coefficients between the profiles obtained by the OISI intensity profile and the corresponding depth-integrated fOCT intensity profile obtained from 6 different scan positions of a single cat

Scan position index	Correlation for 0–90°	Correlation for 45–135°
Position 1	0.58	0.65
Position 2	0.32	0.29
Position 3	0.24	0.39
Position 4	0.89	0.77
Position 5	0.407	0.539
Position 6	0.566	0.559

Next, to investigate what the patches in fOCT maps represent (i.e., whether they represent a localization in the distribution of neurons themselves or a localization of the secondary mechanisms that are behind the origin of the functional signals), we recorded multi-unit activities (MUA) in the scanned region to determine the correlation with the distribution of strength of neuronal activity. MUA recordings were done with glass-coated tungsten electrodes. **Figure 6.10A** shows a representative example of the variation of MUA with respect to the cortical depth for four different grating orientations. As seen from the figure, the stimulus selectivity across a single track is retained. However, the evoked response at different depths is not of the same magnitude and it varies across depth with the response being the largest for a depth of 100–400 μm. This implies that, across the depth, all neurons do not behave in the same way and they have individual characteristics as would be expected from an ensemble of neurons. We would like to emphasize this variation in the evoked response and we expect this variation could be detected by the proposed fOCT measurement.

Figure 6.10B shows an example of the result of a comparison of the fOCT depth profile with the MUA profile. Variation of the fOCT profile generally agrees with the non-uniformity of evoked response across different depths. This suggests that the functional signal measured by fOCT may be correlated with the spiking activity of neurons. A calculation of the correlation coefficient revealed that the profiles are well interrelated. Results of correlation obtained from six different scan positions and three different cats are presented in **Table 6.2A and B**, respectively. Except for two cases, the correlation coefficient was fairly high, indicating that fOCT could indeed measure functional maps.

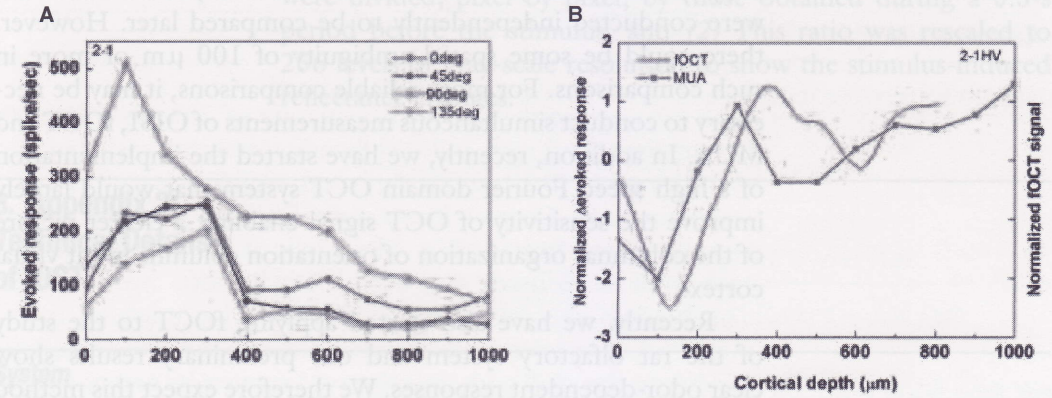

Fig. 6.10. An example of (**A**) MUA-evoked responses as a function of depth obtained from a single track for different orientation stimuli and (**B**) a comparison of difference of the evoked MUA response (shown in red) with the fOCT profile (shown in green) as a function of depth for the difference of 0° minus 90° orientation stimulus. (*See* Color Plate)

Table 6.2
Cross-correlation coefficients obtained from (A) different tracks of a single averaged x–z scan and (B) population result from three different cats

Correlation between fOCT and unit profiles (A)		
Site #	**Correlation coeff. for 0–90 deg**	**Correlation coeff. for 45–135**
#1	0.94	0.66
#2	0.809	0.764
#3	0.908	0.926
#4	0.852	0.899
#5	0.348	0.374
#6	0.751	0.365
(B)		
Cat #	# of sites that show significant correlation ($p<0.005$)	
C-22	4/8	
C-30	9/11	
C-36	5/11	

7. fOCT – Future Prospects

It should be mentioned that in the comparison study discussed in the previous section, different methods of OISI, fOCT and MUA were conducted independently to be compared later. However, there could be some spatial ambiguity of 100 μm or more in such comparisons. For more reliable comparisons, it may be necessary to conduct simultaneous measurements of OISI, fOCT and MUA. In addition, recently, we have started the implementation of a high speed Fourier domain OCT system that would largely improve the sensitivity of OCT signal enabling a clearer picture of the columnar organization of orientation columns in cat visual cortex.

Recently, we have also started applying fOCT to the study of the rat olfactory system and our preliminary results show clear odor-dependent responses. We therefore expect this method to provide novel insights regarding the response distribution in granule cell layers that receive input from olfactory glomeruli and lie deeper from superficial regions of the bulb.

Appendix 1: Technical Details of Functional Retinography

The monkeys were anesthetized by a mixture of 70% N_2O, 30% O_2 supplemented with 1.0–1.5% of isoflurane and were paralyzed with vecuronium bromide (0.1–0.2 mg/ kg/ hour). Before the recordings, the pupils were fully dilated with topical tropicamide (0.5%) and phenylephrine hydrochloride (0.5%). A modified digital fundus camera system (NM-1000, Nidek, Aichi, Japan) was used to observe and measure the light reflectance changes from the ocular fundus. The fundus images were recorded with a CCD camera (PX-30BC, Primetech Engineering, Tokyo, Japan), and the images were digitized with an IBM/PC-compatible computer equipped with a video frame grabber board (Corona II, Matrox, Quebec, Canada: gray level resolution, 10 bits; spatial resolution, 640 x 480; temporal resolution, 1/30 s). The camera was focused on the macular vessels, and the area recorded covered 45 degrees, which included the macula, superior and inferior vascular arcades, and the optic disk.

The fundus was continuously monitored with light from a halogen lamp filtered through a red (610–650 nm) or infrared (840–900 nm) interference filter. Each recording trial consisted of three hundred video frames collected at 30 frames/sec for a total recording time of 10 s. A Xenon flash (duration: 1 msec) was given to the whole posterior pole of the ocular fundus, 500 msec after the initiation of data acquisition. The flash intensity measured at the cornea was 1.54×10^2 cd•s/m^2. The timing of the data acquisition and stimulus delivery was under computer control. Changes in light reflectance from the ocular fundus following the stimulus, such as a darkening (a decrease in light reflectance) or a brightening (an increase in light reflectance), were measured. The optical signal was calculated as follows: *(1)* The gray-scale values of the image obtained after the stimulus were divided, pixel by pixel, by those obtained during a 0.5-s period before the stimulus, and *(2)* This ratio was rescaled to 256 levels of gray-scale resolution to show the stimulus-induced reflectance changes.

8. Appendix 2: *Technical Details of fOCT*

System

We used a fiber-based OCT imaging system (**Fig. 6.7B**). It consists of a Mach-Zehnder-type heterodyne interferometer

constructed from single-mode fibers for flexibility. Light from a broadband source (AFC Technologies, Canada) operating at an output power of 30 mW and having a central mean wavelength (λ_0) of 1.31 μm and a spectral width ($\Delta\lambda$) of 50 nm is split into sample and reference beams in the respective ratio of 19:1 by coupler 1. Optical frequencies of the sample and reference beams are shifted by acousto-optic modulators (AOM, Asahi glass, Japan). We use AOMs to introduce a constant and stable phase delay between the interfering beams. Both the reference and sample beams, after passing through the circulators, illuminate the reference mirror and cortex, respectively. The reflected lights were recombined at coupler 2. An interference beat signal that has a beat frequency of 250 kHz is detected only when the path lengths of the interferometer arms are matched to within the coherence length of the source that is calculated to be 34 μm in free space. Heterodyne detection was done with a lock-in amplifier (EG&G, USA) and the amplitude of the demodulated components was fed into a computer via a 16-bit A/D converter. The reference mirror M was mounted on a motorized stage and scanned at a speed of 2 mm/sec.

The sample arm viewing the animal side consisted of an objective lens of numerical aperture 0.08 and was also fitted with a CCD camera. This allowed simultaneous viewing of the cortical surface with the introduction of visible light from an auxiliary laser source (wavelength 680 nm). The whole unit was mounted on a manipulator unit (**Fig. 6.7C**) that has five degrees of freedom of translation along three axes and rotation and tilt (the flexibility is needed for making the probing light beam normal to the cortical surface). Galvano scanners were installed so as to perform surface scans. The animal-related fluctuation in the signal was reduced by conducting measurements in synchronization with heartbeat and respiration and by keeping the brain surface immobile using agarose.

Animals and Surgery

Each cat was anesthetized with a mixture of 70% N_2O and 30% O_2 supplemented with 1–2% isoflurane, paralyzed with Pancuronium bromide (0.1 mg/Kg/hr), and artificially ventilated by a respirator unit. Contact lenses were fitted to the eyes to protect the cornea from drying. The pupils of the eyes were dilated with 0.5% tropicamide and 0.5% phenylephrine hydrochloride. The head of the animal was held tightly by attaching it to a metal rod. A stainless steel chamber (18 mm inner diameter) was fixed onto the skull with dental acrylic cement by aseptic surgery and was placed above area 18 (coordinates A10P5 of Horsheley). After removal of the dura mater, the inside of the chamber was

filled with 1.2% agarose (Agarose-HGS, Nacalai tesque, Japan, gel strength 1.5%) containing dexamethasone and antibiotics and was sealed with a round glass cover slip and a silicon gasket. Rectal temperature, ECG and expired CO_2 were continuously monitored during both OCT experiments and surgery.

OCT Scan

The stimuli were the same as that used for OISI and consisted of square-wave gratings (white = 8 cd/m2, black=0 cd/m2) having a spatial frequency and moving at a velocity of 4 degrees/sec. The stimulus set consisted of five patterns with control or blank (mean luminance 4 cd/m^2), horizontal (0°), vertical (90°) and oblique gratings (45°, 135°) and were presented in a random order. All stimuli were generated with a VSG2/3 graphics video board (Cambridge Research Systems, UK). The center of the visual field was roughly estimated by projecting images of optic discs onto a screen in front of the animal. The distance of the CRT screen (200–300 mm) was adjusted to have the best focus of optic discs and surrounding vessel patterns. A total of 40 trials were obtained for each stimulus. In a single trial, data acquisition was done for 8 s, during which time 16 *x*-*z* frames (128×100 pixels corresponding to 1 × 1 mm) were obtained. The inter-stimulus interval (ISI) was 5 s. A schematic is shown in **Fig. 6.7D**. Stimuli appeared with a delay of 2 s after the acquisition onset and persisted for 2 s.

OCT Data Correction and Analysis

First, the scans were corrected for any misalignment of the surface position by a correlation-based procedure. For a single stimulus, we obtained a total of 640 scans. To compensate for the small variations in the surface position over different scans, we used correlation analysis. Out of these 640 scans, we selected an arbitrary scan (i) with the reflectivity detected as a function of depth being $R_s(x,z,i)$ at a lateral position x for a stimulus s. Next, we calculated the correlation between the ith scan and rest of the scans (j) using the following equation:

EMBED Equation.DSMT4

$$\Omega(\Delta z; i, j) = \frac{\int_{-\infty}^{\infty} R_s(x, z, i) R_s(x, z + \Delta z, j) dz}{\sqrt{\int_{-\infty}^{\infty} R_s(x, z; i) dz \int_{\infty}^{\infty} R_s(x, z + \Delta z; j) dz}} \quad (6.1a)$$

This operation gives the position of the correlation peak that corresponds to the amount of shift necessary for the jth profile to be in alignment with the ith profile.

Pixel noise was removed with a smoothing filter of window size 27 ×21 μm.

Next, the ratio of the post-stimulus over pre-stimulus scans was calculated for all the grating stimuli and the control condition as follows:

$$\gamma_s(x,z,t) = \frac{R_s^{post}(x,z,t)}{\Sigma_{Prescans} R_s^{Pre}(x,z,t)} \quad (6.2)$$

Here R_s is the reflectivity at position (x, z) at time t. "post" and "pre" indicate post-stimulus and pre-stimulus scans. The division operation removes the unchanging common variation and extracts only changes due to visual stimulation. Next, the ratio was averaged for all the scans obtained for each stimulus $< \gamma_s(x,z) >$. Finally, the differential OCT signal $< \gamma_{diff}(x,z) >$ was calculated as,

$$< \gamma_{diff}(x,z) > = < \gamma_{grating}(x,z) > - < \gamma_{control}(x,z) > . \quad (6.3)$$

With the above equation, by subtracting the differential OCT signal of the control, we could remove noise fluctuations such as respiration artifacts that were locked to the recording but not to the grating stimulus . We have restricted this discussion mainly to the results obtained by calculating the difference between $<\gamma_s$ (x,z)> that were obtained for two orthogonal gratings. The spatial map has been smoothed with a moving average filter roughly 100×115 μm.

References

1. Blasdel, G.G. and Salama, G. (1986) Voltage-sensitive dyes reveal a modular organization in monkey striate cortex. *Nature* 321 (6070), 579–585
2. Grinvald, A. et al. (1986) Functional architecture of cortex revealed by optical imaging of intrinsic signals. *Nature* 324 (6095), 361–364.
3. Ts'o, D.Y. et al. (1990) Functional organization of primate visual cortex revealed by high resolution optical imaging. *Science* 249 (4967), 417–420.
4. Bonhoeffer, T. and Grinvald, A. (1991) Iso-orientation domains in cat visual cortex are arranged in pinwheel-like patterns. *Nature* 353 (6343), 429–431.
5. Malonek, D. et al. (1994) Optical imaging reveals the functional architecture of neurons processing shape and motion in owl monkey area MT. *Proc R Soc Lond B Biol Sci* 258 (1352), 109–119.
6. Roe, A.W. and Ts'o, D.Y. (1995) Visual topography in primate V2: Multiple representation across functional stripes. *J Neurosci* 15 (5 Pt 2), 3689–3715.
7. Wang, G. et al. (1998) Functional architecture in monkey inferotemporal cortex revealed by in vivo optical imaging. *Neurosci Res* 32 (1), 33–46
8. Uchida, N. et al. (2000) Odor maps in the mammalian olfactory bulb: Domain organization and odorant structural features. *Nat Neurosci* 3 (10), 1035–1043.
9. Tsunoda, K. et al. (2001) Complex objects are represented in macaque inferotemporal cortex by the combination of feature columns. *Nat Neurosci* 4 (8), 832–838.
10. Vanzetta, I. and Grinvald, A. (1999) Increased cortical oxidative metabolism due to sensory stimulation: Implications for functional brain imaging. *Science* 286 (5444), 1555–1558
11. Vanzetta, I. et al. (2004) Columnar resolution of blood volume and oximetry functional maps in the behaving monkey; implications for FMRI. *Neuron* 42 (5), 843–854

12. Fukuda, M. et al. (2005) Localization of activity-dependent changes in blood volume to submillimeter-scale functional domains in cat visual cortex. *Cereb Cortex* 15 (6), 823–833
13. Tsunoda, K. et al. (2004) Mapping cone- and rod-induced retinal responsiveness in macaque retina by optical imaging. *Invest Ophthalmol Vis Sci* 45 (10), 3820–3826
14. Hanazono, G. et al. (2007) Intrinsic signal imaging in macaque retina reveals different types of flash-induced light reflectance changes of different origins. *Invest Ophthalmol Vis Sci* 48, 2903–2912
15. Bowmaker, J.K. et al. (1980) Microspectrophotometric demonstration of four classes of photoreceptor in an old world primate, Macaca fascicularis. *J Physiol* 298, 131–143
16. Kilbride, P.E. et al. (1983) Determination of human cone pigment density difference spectra in spatially resolved regions of the fovea. *Vision Res* 23 (12), 1341–1350
17. Kilbride, P.E. et al. (1989) Human macular pigment assessed by imaging fundus reflectometry. *Vision Res* 29 (6), 663–674
18. Elsner, A.E. et al. (1993) Mapping cone photopigment optical density. *J Opt Soc Am A* 10 (1), 52–58
19. Mandelbaum, J. and Sloan, L.L. (1947) Peripheral visual acuity. *Am J Ophthalmol* 30, 581–588
20. Birch, D.G. et al. (1987) The relationship between rod perimetric thresholds and full-field rod ERGs in retinitis pigmentosa. *Invest Ophthalmol Vis Sci* 28 (6), 954–965
21. Pulos, E. (1989) Changes in rod sensitivity through adulthood. *Invest Ophthalmol Vis Sci* 30 (8), 1738–1742
22. Osterberg, G. (1935) Topography of the layer of rods and cones in the human retina. *Acta ophthalmol* 13 (Suppl 6), 6–97
23. Curcio, C.A. et al. (1987) Distribution of cones in human and monkey retina: Individual variability and radial asymmetry. *Science* 236 (4801), 579–582
24. Packer, O. et al. (1989) Photoreceptor topography of the retina in the adult pigtail macaque (Macaca nemestrina). *J Comp Neurol* 288 (1), 165–183
25. Sutter, E.E. and Tran, D. (1992) The field topography of ERG components in man – I. The photopic luminance response. *Vision Res* 32 (3), 433–446
26. Weinhaus, R.S. et al. (1995) Comparison of fluorescein angiography with microvascular anatomy of macaque retinas. *Exp Eye Res* 61 (1), 1–16
27. Bonhoeffer, T. and Grinvald, A. (1996) Optical Imaging Based on Intrinsic Signals: The Methodology. In *Brain Mapping* (Toga, A.W. and Mazziotta, J.C., eds.), pp. 55–97, Academic Press, New York
28. Yao, X.C. et al. (2005) Rapid optical coherence tomography and recording functional scattering changes from activated frog retina. *Appl Opt* 44 (11), 2019–2023
29. Bizheva, K. et al. (2006) Optophysiology: depth-resolved probing of retinal physiology with functional ultrahigh-resolution optical coherence tomography. *Proc Natl Acad Sci U S A* 103 (13), 5066–5071
30. Srinivasan, V.J. et al. (2006) In vivo measurement of retinal physiology with high-speed ultrahigh-resolution optical coherence tomography. *Opt Lett* 31 (15), 2308—2310
31. Huang, D. et al. (1991) Optical coherence tomography. *Science* 254 (5035), 1178–1181
32. Bouma, B.E. and Tearney, G.J. (2002) *Handbook of Optical Coherence Tomography*, Marcel Dekker Inc.
33. Malonek, D. et al. (1997) Vascular imprints of neuronal activity: relationships between the dynamics of cortical blood flow, oxygenation, and volume changes following sensory stimulation. *Proc Natl Acad Sci U S A* 94 (26), 14826–14831
34. Tomita, M. et al. (1983) Effects of hemolysis, hematocrit, RBC swelling, and flow rate on light scattering by blood in a 0.26 cm ID transparent tube. *Biorheology* 20 (5), 485–494
35. Holthoff, K. and Witte, O.W. (1998) Intrinsic optical signals in vitro: A tool to measure alterations in extracellular space with two-dimensional resolution. *Brain Res Bull* 47 (6), 649–655
36. Rajagopalan, U.M. et al. (2003) Functional optical coherence tomography to reveal functional architecture of cat visual cortex in vivo. In *Proceedings of SPIE* (Vol. 5140), pp. 77–83
37. Maheswari, R.U. et al. (2003) Novel functional imaging technique from brain surface with optical coherence tomography enabling visualization of depth resolved functional structure in vivo. *J Neurosci Methods* 124 (1), 83–92
38. Lazebnik, M. et al. (2003) Functional optical coherence tomography for detecting neural activity through scattering changes. *Opt Lett* 28 (14), 1218–1220
39. Hubel, D.H. and Wiesel, T.N. (1977) Functional architecture of macaque monkey visual cortex. *Proc R Soc Lond B Biol Sci* (198), 1–59
40. Rajagopalan, U.M. et al. (1999) An optical coherence tomographic imaging system for investigating cortical functional

organization of brain: A simulation study. In *The International Society for Optical Engineering* (Vol. 3749), pp. 400–401
41. Bonhoeffer, T. and Grinvald, A. (1993) Optical imaging of the functional architecture in cat visual cortex: the layout of direction and orientation domains. *Adv Exp Med Biol* 333, 57–69
42. Hanazona, G. et al. (2008) Evaluating neural activity of retinal ganglion cells by flash-evoked intrinsic signal imaging in macaque retina. *Invest ophthalmol vis sci* in press

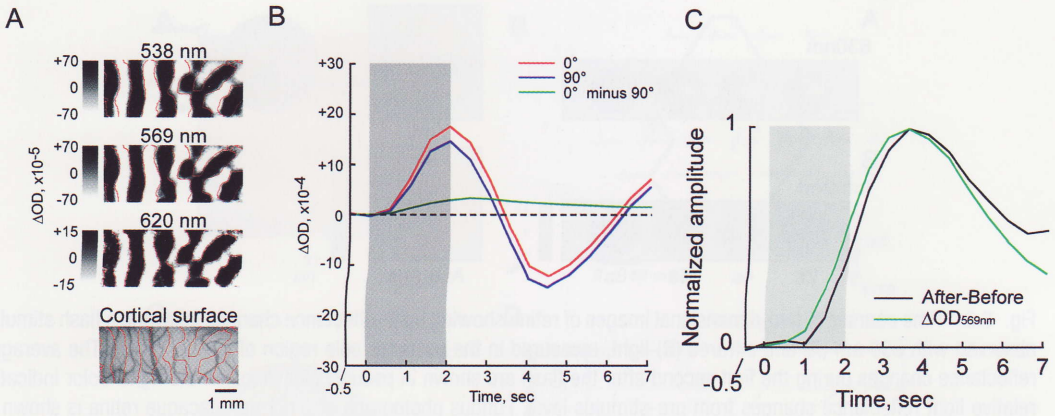

Fig. 6.1. Orientation columns visualized by OISI at different wavelengths. Typically in visual cortex, intrinsic signals consist of stimulus-specific and -nonspecific components. Orientation columns are reflected in the stimulus-specific component that is a local modulation of a stimulus-nonspecific component. In (A), we subtracted activation patterns obtained by one stimulus (90 deg. orientation) from the other (0 deg. orientation) to remove stimulus-nonspecific components. Please note that, depending on the size of the functional structures of interest, stimulus specificity of synaptic inputs, and spread of intrinsic signals, distinction between stimulus-specific and nonspecific components may not be required (for example, see **Figs. 6.3 and 6.4**). Columnar patterns obtained at different wavelengths are nearly the same as indicated by contours in red drawn for columnar patterns obtained at 620 nm. Although it is not shown here, similar patterns of functional structures were also observed using infrared light. Bottom image shows vessel patterns of the exposed cortical surface where the above recordings were made. (B) Time courses of stimulus-nonspecific (red and blue lines) and stimulus-specific (green line) components obtained at 620 nm. The visual stimulus was given from 0 to 2 s. (C) Time course of stimulus-nonspecific components obtained at 570 nm (Green line). The black line indicates time course estimated by subtraction between time courses obtained before and after the extrinsic absorption dye infusion (see Fukuda et al., 2005 for details). The visual stimulus was given from 0 to 2 s.

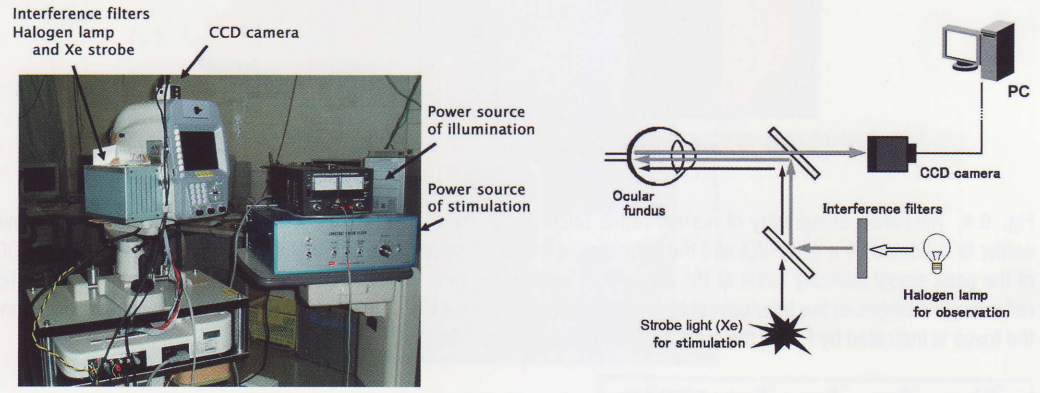

Fig. 6.2. Overall view of the intrinsic signals imaging system for retina (left) and schematic drawing of the experimental setup (right). Throughout the recording trial, the fundus was continuously illuminated with observation light through one of the bandpass filters.

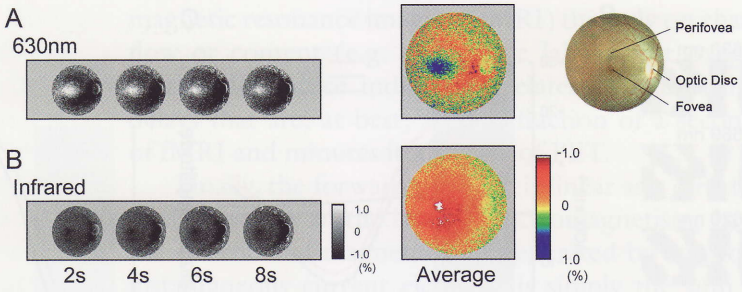

Fig. 6.3. Time courses of two-dimensional images of retina showing light reflectance changes following a flash stimulus observed with 630 nm (**A**) and infrared (**B**) light, measured in the posterior pole region of normal retina. The averaged reflectance changes during the first second after the flash are shown in pseudocolor maps on the right. Color indicates relative light reflectance changes from pre-stimulus level. Fundus photograph of a normal macaque retina is shown in the right.

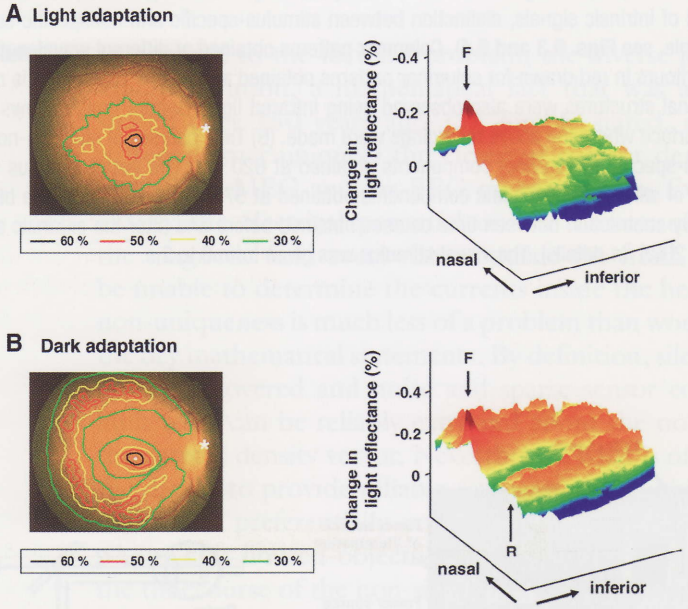

Fig. 6.4. Response topography of normal retina under light-adapted (**A**) and dark-adapted (**B**) conditions. The foveal center is indicated by a white dot and the optic disk is indicated by an asterisk. Regions with 60%, 50%, 40% and 30% of the peak signal intensity value at the fovea were outlined by different colors. Pseudocolor topographic maps of light reflectance changes in the inferior retina, profiled along the horizontal meridian, are shown on the right. The location of the fovea is indicated by F, and the crest of 'rod ring' is indicated by R.

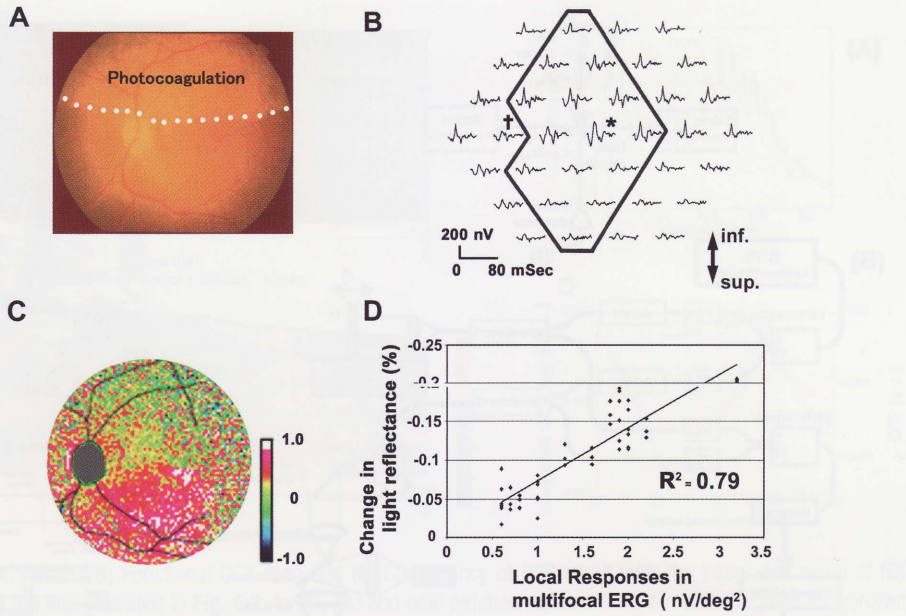

Fig. 6.5. (**A**) Photograph of the monkey's retina artificially damaged by Argon Laser Photocoagulation. The upper half of posterior retina was densely coagulated, sparing the macular area. (**B**) Array of 37 local responses of multifocal ERG, taken from the fundus in (**A**). ERGs with ∗ and † indicate the location of macula and optic disk, respectively. Note that the responses of the intact retina in the lower half region are inversely shown in the upper half of the arrays. (**C**) pseudocolor map of flash-evoked intrinsic signals measured with infrared light. Red color indicates light reflectance decrease (*darkening*) from pre-stimulus level. Flash-evoked darkening could not be observed in the damaged region (*upper half*). (**D**) Correlation between the change in light reflectance decrease and the focal responses in ERG at the corresponding retinal location under infrared light. Correlation coefficient: $r^2 = 0.79$ ($p < 0.001$, $n=45$).

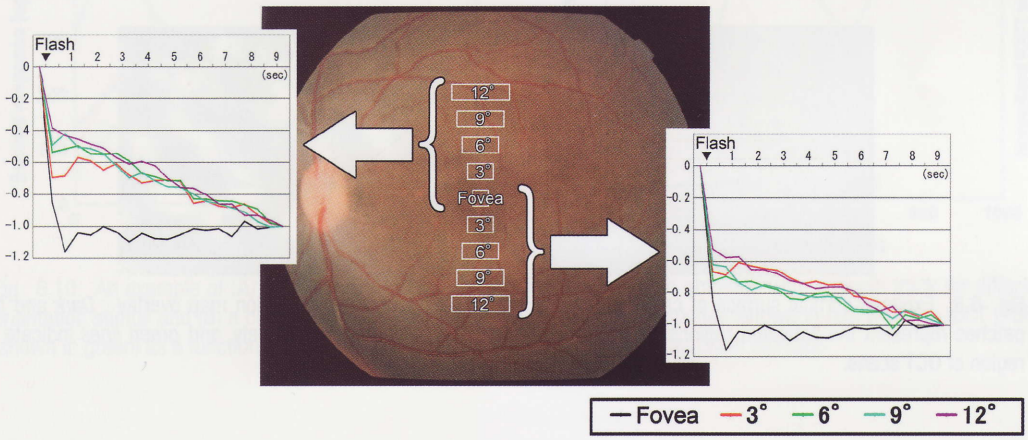

Fig. 6.6. Time courses of light reflectance changes in a single trial following a diffuse flash, measured at the fovea and different regions within twelve degrees superior or inferior to the fovea. Amplitudes are indicated as values relative to the light reflectance changes at the end of each trial (1.0). The four regions tested in each quadrant are indicated as distances from the fovea (3,6,9 and 12°).

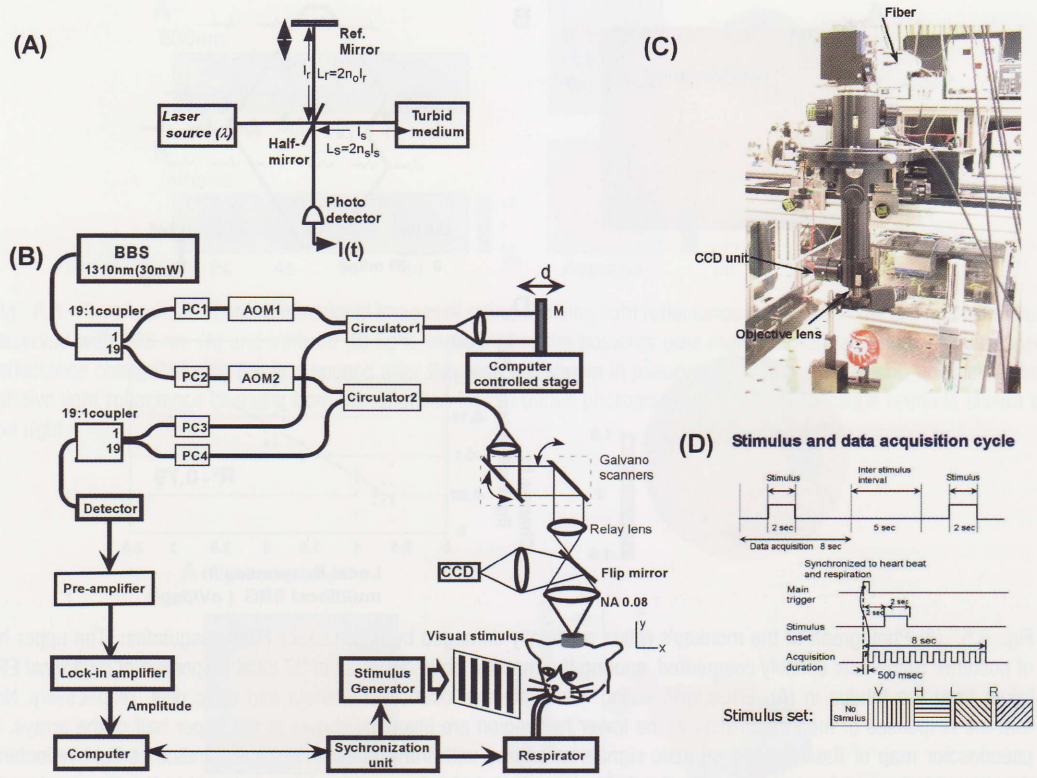

Fig. 6.7. A schematic of the basic principle of OCT (**A**) and the experimental system used (**B**) along with a picture of the probe unit (**C**) and a schematic of the scanning paradigm (**D**). In the figure (**B**), the abbreviations denote: BBS - Broad Band Source, AOM- Acousto-Optic Modulator, PC - Polarization Controller, M – Mirror and O – Objective lens.

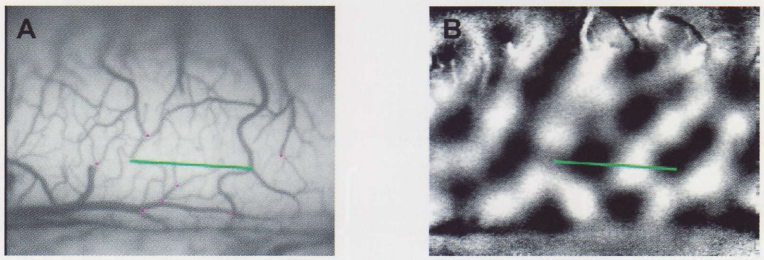

Fig. 6.8. Exposed cortical surface of cat visual cortex with (**B**) a thresholded activation map overlay . *Dark* and *light* patches represent the activated regions for horizontal and vertical gratings, respectively, and *green lines* indicate the region of OCT scans.

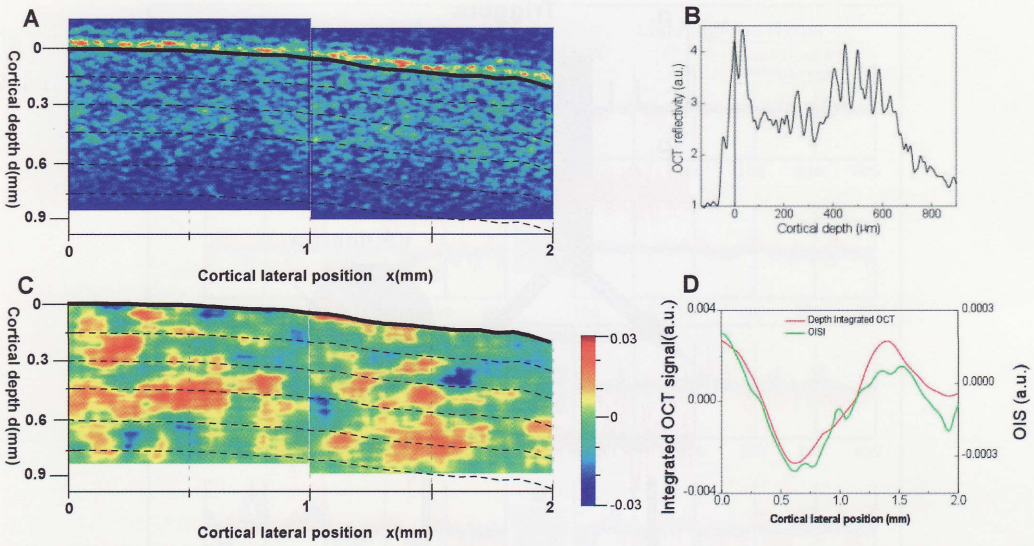

Fig. 6.9. (**A**) OCT scan, (**B**) Functional OCT map and (**C**) Consistency of OISI result with the integrated result of fOCT obtained across the line indicated in **Fig. 6.2**. In (**B**), *red* and *blue* patches represent the activated regions for horizontal and vertical gratings, respectively. Green line indicates the variation of OISI across the line indicated in **Fig. 6.2B**. In the graph (**C**), *red line* obtained by calculating the functional signal from integrating the OCT scans across the full scanned depth range of **Fig. 6.3B** while green line indicates the intensity variation across the green line of **Fig. 6.2B**.

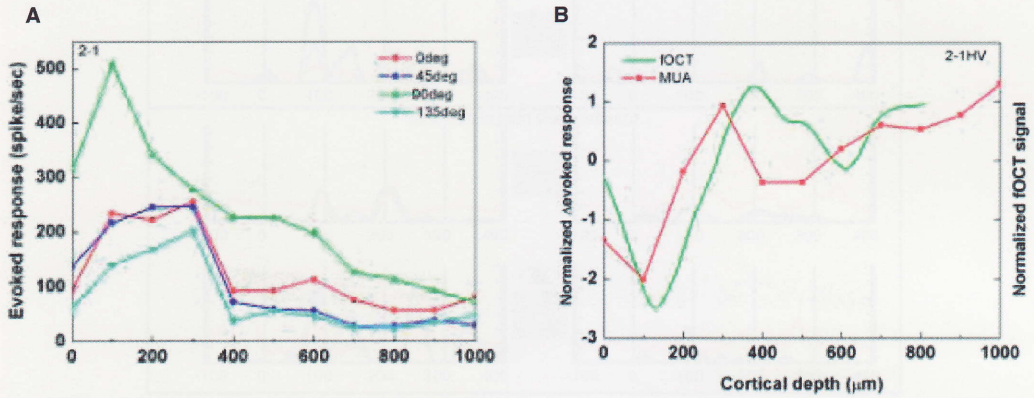

Fig. 6.10. An example of (**A**) MUA-evoked responses as a function of depth obtained from a single track for different orientation stimuli and (**B**) a comparison of difference of the evoked MUA response (shown in red) with the fOCT profile (shown in green) as a function of depth for the difference of 0° minus 90° orientation stimulus.